doi:10.1038/nature20571

Contents

I. Supplementary Discussion

Here, we provide further conceptual details and analyses regarding the EF-X method.

A. Electric fields and protein crystals

The electric fields required for EF-X are large by laboratory standards: a field of 1 MV/cm corresponds to the imposition of 10,000 volts across a 100 µm crystal (which we will use as a reference thickness). Such voltages pose a number of challenges informing our experimental design. Most fundamentally, protein crystals - like any material - can suffer dielectric breakdown under electric field pulses. Given the dense, wet nature of protein crystals, ionization avalanches are unlikely to occur since charged particles cannot be accelerated sufficiently between collisions. Rather, the main two pathways to dielectric breakdown that appear to be relevant are (a) mechanical pressure and (b) ohmic heating. We consider these individually below.

Mechanical pressure results from the Coulombic attraction between accumulating charges on both sides of the crystal. Assuming that the capacitance C of a protein crystal can be modeled as that of a parallel plate capacitor, we can write $C = \frac{\epsilon A}{d}$ where ϵ is the dielectric permittivity of the crystal, A is its surface area, and d its thickness. The pressure due to the electric field is $-\frac{1}{2}\epsilon E^2$ where E is the electric field strength. That is, the field will compress the crystal in a manner dependent on the field strength and relative permittivity (since $\epsilon = \epsilon_r \epsilon_0$) of the crystal. Estimated ϵ_r are ~ 12 for hemoglobin[1] and ~ 37 for monoclinic lysozyme crystals[2]. Taking the latter yields $P = 1.6$ MPa at 1 MV/cm. Lysozyme crystals can tolerate hydrostatic pressure up to 1 GPa[3,4], and have a yield stress under point-like

pressure along the [1 1 0] direction of $5 - 10$ MPa[4].

Ohmic heating results from ionic currents running through the crystal's solvent channels. Molecular dynamics simulations[5] suggest that protein crystals obey Ohm's law up to large field strength, i.e. $V = IR$, where V is the applied voltage, I is the resulting current, and R is the crystal series resistance. The resulting power dissipation, $P = VI$ results in a temperature jump $\Delta T = P\tau/C_p$, where τ is the pulse duration of the applied field and C_p is the crystal heat capacity. This temperature jump can be expressed in intrinsic terms as $\Delta T = E^2\tau\sigma/c_p$ where σ is the conductivity of the crystal, related inversely to its resistance ($R = \frac{d}{\sigma A}$), and c_p here defined as its heat capacity per unit volume.

What all this means is that, given the desired field strength, the heating rate is independent of crystal shape but will be linearly dependent on electric field duration and conductivity. Indeed, the anticipated heating rate is large. For lysozyme, under the conditions at which measurements have previously been made[6], we estimate that $\frac{\Delta T}{\tau} \sim 2 \times 10^7$ K/s at 1 MV/cm. Removing salt from protein solutions (or protein crystals) reduces crystal conductivity further by 30-50 fold (data not shown). Many crystallization agents, such as poly(ethylene glycol), increase viscosity substantially, often further reducing conductivity. Under these conditions, heating is irrelevant for crystals with conductivities like lysozyme on submicrosecond time scales. We note that crystal cooling by thermal diffusion takes place on the millisecond to second time scale (estimated thermal equilibration time scale of 50-100 ms[7]).

Typically, protein crystals have much lower conductivity than their corresponding crystallization solutions (lysozyme: 50-200 fold[6]). This means, that, in order to minimize heating, all current should flow through the crystal and not around it. To this end, we mount protein crystals across the orifice of capillaries (Figure 1c-d): the only conductive path runs through the crystal. The crystal is attached by coating the junction with the electrode tip with Sylgard 184 (Dow-Corning Inc.), a dielectric elastomer. Another harmful effect of an applied electric field is the occurrence of electrolysis at the electrodes, leading to gas bubble formation. Such electrolysis is proportional to current (Faraday's first law of electrolysis), and appears in our experiments to be adequately minimized by a proper electric seal around the protein crystal. Thus, Sylgard-based gluing of crystals serves a dual purpose: electric insulation and mechanical stability of the crystal on the electrode.

We note that the placement of thin dielectric insulators between the protein crystal and electrodes is likely not a good experimental choice for the EF-X experiment: dielectric screening by mobile charges (ions) would dramatically decrease the electric field experienced by the protein crystal. In other words, current must flow, with the protein crystal as the least conductive element of the circuit. The resistance between electrodes and crystal also determines how fast the voltage rises across the crystal. For a hypothetical $100 \times 100 \times 100$ μm lysozyme crystal in contact with a solution with conductivity of 1 mS/cm, the expected capacitance (C) is 0.03 pF, with access resistance (R) for a 100 μm liquid junction of 100 kΩ, giving an expected rise time of $RC = 3$ ns. Voltage rise times will be studied in more detail in future work.

Finally, transient electric fields in some cases lead to electrostrictive motion, especially of crystallization solution surrounding the crystal. Such motions were sometimes visible by live video and in one case resulted in visible splitting of spots within the diffraction pattern when exposed with multiple X-ray pulses. Any such motion is likely negligible *during* X-ray pulses, but can lead to displacement *between* X-ray pulses. In principle, such motion does not pose a problem for data reduction since geometry of the setup and crystal is refined for each frame - as long as diffraction spots remain intact. The data presented here, however, were based on single X-ray pulses per frame, a straightforward approach for eliminating concerns about the effects of such motion.

B. Statistical validation

Conventionally, difference electron density (DED) maps resulting from time-resolved crystallography are assessed by peak heights, expressed in standard deviations (σ) from the mean. We will present such an analysis below. Usually, signal is concentrated around an optically excitable group. Here, however, any part of the protein can be excited (note that 27 out of 95 residues have charged side chains) and solvent content is somewhat low (40%). As a consequence, our internal DED maps do not contain large "internal negative control" regions that stabilize the overall statistics. For this reason, we present a number of additional analyses, in both real and reciprocal space. We emphasize that data without the electric field (OFF) and at the different time points (ON: 50, 100 and 200 ns; see Figure 2 for experimental design) have similar completeness, R_{merge} and redundancy. The data were acquired in an interleaved manner and scaled together to ensure cancellation of systematic errors throughout the analysis.

Test 1. First, we expect reflections F^{ON}_{hkl} and $F^{ON}_{\bar{h}k\bar{l}}$ to deviate from F^{OFF}_{hkl} and $F^{OFF}_{\bar{h}k\bar{l}}$, respectively, in opposite directions and therefore to be negatively correlated. This is indeed the case, most prominently at 100 and 200 ns (Extended Data Figure 7a-c). Consistent with such correlation, we expect an increase in the variance of $\Delta F = F_{hkl} - F_{\bar{h}k\bar{l}}$ relative to variance due to measurement error alone, and therefore a corresponding increase in map variance (by Parseval's theorem). Ignoring, for simplicity, the role of weighting of reflections in difference map construction and anisotropy correction (for both, see Methods), we expect a relative increase of standard deviation of $1 - 2\rho$, where ρ is the average correlation coefficient calculated in Extended Data Figure 7a-c (note that $\rho < 0$). Indeed, the overall internal DED map σ increases with the delay from the start of the EF pulse (defining the OFF map standard deviation as 1: 1.099× at 50 ns, 1.244× at 100 ns, and 1.311× at 200 ns), consistent with this expectation.

Test 2. Second, the ON internal DED map, ideally, has higher peaks and lower valleys than the internal DED of the OFF map. Such DED is likely also distributed less uniformly throughout the unit cell and thus expected to lead to "heavy tails" in the distribution of DED values. We therefore looked for systematic deviations from a normal distribution in the tails of the internal DED distribution over voxels (for the OFF data, we expect the central limit theorem to apply). Indeed, the excess number of voxels with large deviations from 0 increases with the delay from the start of the EF pulse in internal DED maps (Extended Data Figure 7g-j), and progressive, statistically significant deviations from a normal distribution appear, as assessed by three different statistical tests (Extended Data Figure 7, legend). These tests are independent of **Test 1** above.

Test 3. Third, we do have some expectations of where difference electron density peaks will be localized. Preliminary molecular dynamics simulations (unpublished) and initial data both indicated that strong DED map peaks are to be expected around backbone oxygen atoms. Such a pattern is not unexpected given the number of electrons of oxygen (8) compared to carbon (6) and nitrogen (7), their low B-factors compared to side chain atoms, and relatively high spatial contrast (they are the "pointiest" features of the protein backbone). To perform a test independent of the previous two, we ask what fraction of observed peaks above 3.5 σ or below -3.5 σ, fall within a 1.5 Å radius of backbone oxygen atoms (due to voxelization, at 0.3 grid spacing, the effective probe volume radius is 1.80 Å; analysis in UCSF Chimera). These probe volumes occupy 10.4% of the unit cell. The threshold of 3.5 σ was chosen as the point where the voxel internal DED distribution (Extended Data Figure 7g-j) starts to deviate clearly from normality. At 100 and 200 ns, we find significant localization of internal DED near backbone oxygen atoms (Table S4). More generally, it is customary to examine the location and strength of the strongest difference map features (200ns: Table S5, OFF: Table S6). We find that the strongest internal DED peaks are found preferentially near the protein backbone ($p < 0.01$) and charged residues ($p < 0.05$), another natural expectation.

Test 4. Fourth, signal is likely to have a larger typical spatial extent than noise. Motions of nearby atoms are expected to be correlated and thus to result in clustering of difference electron density. As a result, using larger sampling volumes should average out noise faster than signal. To specifically assess the clustering of internal DED near the protein backbone, as apparent from Figure 3b, we integrate the absolute value of internal DED above 2.5 σ (as illustrated as the "signal" in Figure 3a). In Figure 3g, we did implicitly assume that OFF and ON data sets are subject to the same measurement errors. This is quite likely given that OFF and ON diffraction patterns were acquired in an interleaved manner and show similar completeness, redundancy and R_{merge} (Table S3), and also consistent with the increase in map standard deviation as reviewed above. However, to be conservative, we consider here the case of an unknown source of additional error causing, instead, the entire increase in internal DED map standard deviation. To do so, we compare signal per residue to random sampling from the unit cell of the OFF internal DED map using equal sized probe volumes (that is, we quantify false-positive signal, Extended Data Figure 7d-f). For this additional error scenario, we lower the sampling threshold to $2.5\ \sigma_{OFF} \times (\sigma_{OFF}/\sigma_{ON})$, after which we multiply the false positive signal by σ_{OFF}/σ_{ON} for comparison with the ON data. To judge the statistical significance of the traces in Figure 3g, we use the 95$^{\text{th}}$ percentile obtained by this random sampling protocol. As shown in Extended Data Figure 7d-f, we find substantial signal even above this conservative threshold for 13 residues at 50 ns ($p = 9 \times 10^{-4}$), 15 residues at 100 ns ($p = 7 \times 10^{-5}$) and 26 residues at 200 ns ($p < 10^{-12}$).

Test 5. Finally, of course, are the data reproducible? The presented data set is the best one we have acquired to date, with other data sets having lower completeness and redundancy. To make a comparison, we merged data from two other crystals (for statistics, see Table S7). We find that both structure factor differences and internal structure factor differences are moderately correlated between data sets, with high statistical significance (Extended Data Figure 7k-l).

C. A note on structural model errors

Our refinement strategy is geared towards the accurate refinement of structural differences, rather than overall model accuracy. We start from a high-quality model for the OFF state, based largely on a high-resolution monochromatic data set (see Methods). Use of an OFF state model as a starting point for structure refinement of the excited states (ES) has two effects: (1) Model errors of the OFF and ES models are highly correlated and will mostly cancel out when comparing models, minimizing model error in the estimation of structural changes[8,9]. (2) A model bias will be present in the excited state model, but this will be the most conservative bias possible: towards not observing conformational change. In other words, we essentially perform difference refinement[10,9] against extrapolated structure factors[11,12]. To minimize spurious modification of the excited state model (ESM), we performed mostly manual refinement in Coot and only slight xyz refinement in PHENIX (automated refinement with geometric constraints). We judge the validity of the ESM in a number of ways.

First, the stepwise decrease in R factors (Extended Data Figure 4a) suggests that most refined structural changes are well supported. With respect to the somewhat large R factor values, we note that these consist of two components: measurement error and model error (that is, $F_o - F_c = (F_o - F_{true}) - (F_c - F_{true})$). Usually, R factors are dominated by model error[9]. Extrapolated structure factors, however, have a large associated effective measurement error, making the magnitude of associated R factors an unreliable measure of model quality. However, the measurement error component stays constant during refinement, such that changes in R_{work} and R_{free} can guide refinement. Secondly, we calculated $2mF_o - DF_c$ composite omit maps (with iterative refinement). We find that most refined structural changes are well supported by these maps. We provide the $2mF_o - DF_c$ maps and composite omit maps calculated with iterative refinement in the Supplementary Online Materials. Thirdly, the refined structural changes explain the features observed in the internal difference maps (Figure 3), which, again, can be calculated without any refinement.

Finally, one can ask how well the ESM explains additional data. First, can the ESM explain an independent data set (data set 2, described under Test 5 above)? To judge this, we directly compare the model to data set 2 (Table S7). We do so without refinement (apart from bulk solvent scaling) such that all 11,129 reflections act as the test set. At low extrapolation factor, the ESM model and an upside-down ESM, obtained by rotation by 180° around the C2 crystallographic y axis, explain the data nearly equally well, both much worse than the OFF model, consistent with the observation that the OFF state dominates overall electron density (Extended Data Figure 4b; note also that the OFF model has not been refined against noisy extrapolated structure factors, giving it an inherent advantage). At high extrapolation factor (> 9), however, the relation inverts and the ESM, but not the rotated ESM, explains the extrapolated structure factors for the second data set better than the OFF model. Second, when comparing the 200 ns ESM model to the 100 ns time point obtained concurrently from the same crystal, we observe nearly identical behavior (Extended Data Figure 4c). Note that, while the improvements over the OFF model are modest (2-3% in both cases), these differences are highly significant given the size of the test set ($N_{refl} > 11,000$ in both cases; standard errors in R_{free} are approximately $\frac{R_{free}}{\sqrt{N_{refl}}} \approx 0.0095 R_{free}$ (ref.[13]; this estimate is likely conservative here given that the measurement error component of R_{free} is fixed for a given extrapolation factor).

D. General applicability of EF-X

Electric fields act on partial and elementary charges, as present naturally in proteins, or as introduced by mutation, change in pH and chemical modification. As such, EF-X has the potential to extend the reach of time-resolved crystallography beyond the few proteins with optically excitable co-factors (most notably hemoglobin[14], myoglobin[15] and photoactive yellow protein[11]). Indeed, EF-X may be a general purpose experiment to explore the functionally relevant excited states of proteins and other biological macromolecules. In this regard, it is important to explain the current experimental conditions that permit the application of EF-X, with a view towards enabling its immediate application and identifying directions for further technical development.

Crystal quality and growth conditions. The point of EF-X is to study protein excited states through introducing and recording subtle but statistically significant perturbations throughout the molecule. As is the case for any comparative study of subtle conformational changes, it is necessary to grow well-diffracting crystals (resolution ≤ 2Å). Indeed, most of the information on structural differences in our data is found in reflections in the resolution range from 2-3 Å (Extended Data Figure 7). Over 40,000 protein structures have been deposited in the PDB with resolutions better than 2.0Å, suggesting wide applicability of EF-X. Another consideration is that crystals grown under high-salt

conditions are not (by empirical observation) immediately amenable to the application of strong electric field pulses. However, preliminary work suggests the viability of a number of strategies to reduce crystal salt content, including the dialysis of protein solutions against glycerol solutions prior to crystallization, the use of "volatile salts" such as ammonium acetate, and the transfer of crystals obtained in high-salt buffers through biphasic aqueous equilibria to polyethylene glycol solutions of similar pH and osmotic pressure[16].

Data collection under electric fields. For protein systems tested to date, we find that individual crystals can withstand hundreds or thousands of electric field pulses of ~1 MV/cm without serious loss of diffraction quality (Extended Data Figure 2, Table S2). However, a key factor (and current challenge) that determines the success rate of this experiment is the control of humidity and osmotic fluctuations during crystal mounting and data collection. Such fluctuations result in physical stresses, increasing crystal mosaicity. This is particularly important given the current use of "pink-beam" Laue diffraction to maximize photons per exposure, a process in which the quality of diffraction is highly sensitive to crystal mosaicity[17]. There are effective approaches for dealing with these issues. The problem of controlling humidity has been effectively addressed for conventional room-temperature crystallography using custom humidity control instrumentation[18] or, more simply, by sustained vapor contact with crystallization solution[19]. In addition, the use of narrow-bandwidth, high-intensity pulsed X-ray sources (e.g. X-ray free electron lasers) should eliminate such concerns altogether, since diffraction of monochromatic X-rays is substantially less sensitive to crystal mosaicity.

Another issue regarding broad application of EF-X is the design of electrodes. Presently, we use manually assembled electrodes with orifices of ~100 μm, requiring the availability of crystals with similarly sized faces to permit mounting. This limitation can be addressed with miniaturization of electrodes, a matter of further engineering. Miniaturization also has the potential to dramatically extend the accessible time scales of investigation (see Extended Data Figure 1).

Symmetry breaking and extent of motions sampled. As described in the main text, a valuable property in the EF-X method is the fact that applied electric fields will generally reduce the symmetry of crystal. Indeed, any crystallographic symmetry operator that does not preserve the electric field vector will be "broken". Thus, processing the data in the appropriate lower symmetry group permits the construction of internal difference Fourier maps between molecules that experience the electric field in different directions. This analysis amplifies the electric field induced effect and isolates this signal from other potential artifactual effects that could arise from crystal heating or radiation damage (which are insensitive to the direction of the electric field).

How general is the property of crystal symmetry breaking? Analysis of the PDB shows that 95% of deposited structures fall within space groups that contain at least one 2, 4, or 6-fold (2n) rotation or screw axis, implying the existence of one or more oppositely oriented asymmetric units (ASUs). Approximately 50% of structures fall in space groups that have (at least) one set of three orthogonal 2n rotation and/or screw axes, meaning that almost any crystal orientation will lead to one or more oppositely oriented ASUs that will experience the electric field in opposite orientations. Thus, symmetry breaking is likely to be a feature shared by most protein crystals. However, we note that the principle of making internal difference maps is even more general than cases involving breaking crystallographic symmetry. For any space group and any crystal orientation, one could simply invert the polarity of the electric field and collect successive diffraction images for the crystal exposed to electric field pulses of opposite orientation. Such a data collection protocol would permit the construction of up - down difference Fourier maps between interleaved datasets of opposite electric field polarity.

An interesting question is the degree to which the electric field applied in just one orientation is expected to sample possible motions in a protein under study. If one assumes transition dipole moments of charges ($\overrightarrow{\Delta\mu}$) to be distributed isotropically, any given electric field orientation $\overrightarrow{E}$ will excite about 50% of motions with at least half the effect achievable by perfect alignment of the electric field with these motions (that is, $\cos(\overrightarrow{\Delta\mu}, \overrightarrow{E}) > 0.5$).

Crystal lattice constraints. An interesting issue is to consider how the crystal lattice might restrict the motions that can be accommodated while retaining crystal integrity. A review of the scientific literature suggests that in many cases, protein function is not limited by assembly into a crystal lattice. For example, a number of enzymes retain catalytic activity in the crystalline state (urease[20], glycogen phosphorylase[21], papain[22], ribonuclease[23,24], DNA polymerase η[25], myoglobin[15], hemoglobin[14,26]). A recent overview of the application of cross-linked enzyme crystals is given in ref. [27]. In addition, Agarwal et al.[28] compared the solution NMR and solid state (crystalline) properties of the SH3 domain of alpha-spectrin and found excellent agreement, both for chemical shifts and R_2 relaxation rates, suggesting detailed preservation of dynamics in the crystalline state. These findings suggest that many important features of protein dynamics might be recapitulated through the study of excited states in protein crystals, a notion

that should be tested more completely in future work.

However, there is no doubt that some protein functions will involve larger-scale conformational changes that could be incompatible with a single crystal state. For such conformational changes, an obvious direction is to carry out "serial EF-X" — a study of excited states in a series of crystals that represent stabilized intermediate states along a functional reaction coordinate. For example, studies in the metabolic enzyme dihydrofolate reductase suggest that such an approach could permit a detailed mapping of a complex, multistate reaction coordinate[29]. The availability of EF-X should now enable this work.

Access to EF-X. Efforts to establish a permanent, generally accessible installation of the EF-X technology are underway at BioCARS (APS).

E. Biological relevance of EF-X

The broad goal of EF-X is to excite and record time histories of motions throughout a protein structure as an approach to deduce the biological reaction coordinate(s). The operating principle is that biologically relevant excited states of proteins are enriched in the low-lying energetic states accessible around the ground state(s). Thus, the kinds of forces imposed by 1 MV/cm fields should be able to bias and expose these states (Extended Data Table 1). Coupled with time-resolved crystallography, this experiment should permit both visualization of relevant excited states and the transitions between them with appropriate spatial and temporal resolution. Here, we show that applied electric fields can indeed drive motions within a protein molecule, that we can observe these motions with atomic resolution, and that the pattern of EF-induced motions significantly overlaps with the pattern of displacements that define the evolutionarily-conserved reaction coordinate in the PDZ domain. However, this study represents an initial analysis of EF-induced motions with just one electric field orientation and at one time scale. That even this partial accounting of induced motions displays association with PDZ function supports the general premise behind EF-X. Nevertheless, it should be understood as a starting point for a larger body of work that will be required for a complete analysis. We outline the essential conceptual and technical issues:

Identifying the biologically relevant motions. Because proteins are marginally stable materials with many degrees of freedom, a full description of their motions will require a high-dimensional representation. Such a description will represents one important goal of EF-X — a systematic cataloging of all the distinct motions over a broad range of time scales that define the basic material properties of a protein. However, it seems likely that the *biologically relevant* motions exist in a much lower dimensional space — a subspace spanned by a small number of evolutionarily-conserved mechanical modes within which a trajectory of orderly, non-random motions defines the reaction coordinate[30]. Another important goal of EF-X is to provide a rigorous test of this conjecture and to determine optimal approaches for identifying and characterizing the relevant mechanical modes. With EF-X, the approach is to collect data (1) at many field orientations and strengths, (2) with and without molecules or mutations that stabilize intermediates along the functional reaction coordinate, and (3) over homologs of a protein family that share a common reaction mechanism. The proposal is that the residues defining the relevant modes will be correlated in perturbations that influence the reaction coordinate and correlated over homologs that share a common design. Because the experiment presented here is at one field orientation and strength in a single wild-type protein, the analysis in Figs. 6b and 6e just compare the magnitudes of motions at each amino acid position — a first-order test that the biologically relevant motions are significantly included in the EF-induced motions. A more complete analysis will come with the development of analytical methods for decomposing the time-dependent correlations in EF-induced motions to identify the collective modes; if correctly done, such a decomposition should separate the majority of idiosyncratic, random motions of atoms from the proposed few conserved, systematic motions that are connected to protein fitness.

The energetic value of interactions. The observation of motions in proteins is not itself a mapping of the forces constraining those motions — the critical information for making physical models for proteins. But, with more development, EF-X can be thought of as a method for mapping the free energy landscape in protein structures at atomic resolution. By varying defined forces with defined orientations and measuring subtle displacements or state transitions of residues, one could collect data required to deduce the spatial pattern of net forces acting between atoms. However, there are several non-trivial issues to address. First, it is important to understand how the externally applied electric field maps to the field within the diffracting volume of the crystal. Second, it must be possible to transform the field within the diffracting volume to the local field experienced by charged species within the unit cell. Finally, it is important to define the groups of atoms that work cooperatively and therefore move in a collective fashion (see

above). These issues represent directions for further study and are made accessible by the development of EF-X.

II. Supplementary Tables

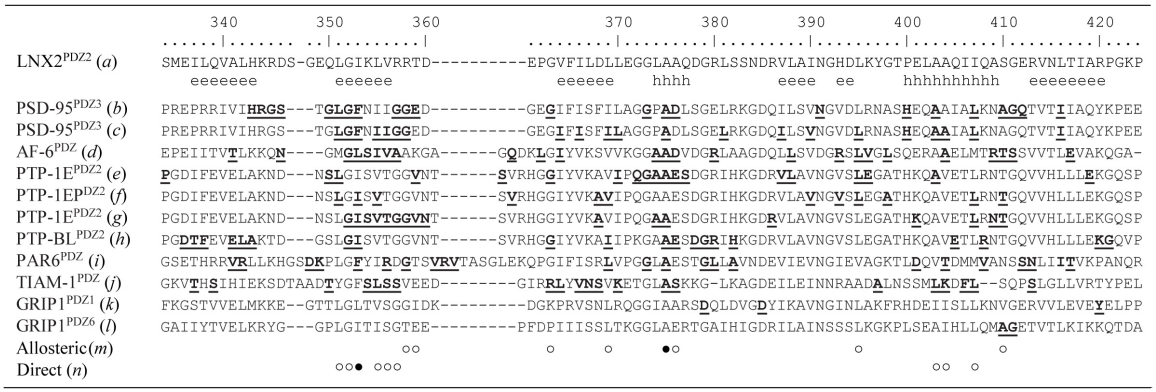

TABLE S1 **Multiple sequence alignment and mapping of results reported in the literature on allostery for PDZ domains**. Selected PDZ domains were aligned based on X-ray structures using Promals3D[31] with limited manual adjustment of gapped regions. Residues significantly affected by allosteric modulatory domains or coupled to ligand binding are indicated (bold and underlined). (a) Sequence of LNX2^{PDZ2}, with residue numbers shown on top and secondary structure underneath (eee..." indicates β strands, hhh... indicates α helix). (b) Sequence of PSD95^{PDZ3} with clusters of residues for which backbone chemical shift in the ligand-bound state respond in a correlated manner to mutations[32]. (c) Residues in PSD95^{PDZ3} for which mutations on average have a significant effect on ligand affinity[33]. (d) Residues in AF-6PDZ with intrinsic millisecond dynamics affected by ligand-binding, or exhibiting millisecond chemical exchange in the ligand-bound state only, or experiencing a substantial change in chemical shift upon ligand binding (Figure 6 and Table 1 of ref. [34]). (e) Residues part of two pathways of energetic correlations identified by molecular dynamics simulations in human PTP-1E^{PDZ2} [35]; (f) Residues of PTP-1E^{PDZ2} displaying a change in dynamics on ligand binding[36], as determined from relaxation dispersion measurements on 13C-labeled methyl groups and backbone order parameters. (g) Residues of PTP-1E^{PDZ2} with chemical shift change ($\Delta\delta > 0.2$) upon binding to Fas receptor C-terminal peptide[37]. (h) Residues of mouse PTP-BL^{PDZ2} showing slow chemical exchange or large chemical shift change upon titration with its modulatory PDZ1 domain, following ref. [38], Figure 3A, and Dr. G. Vuister, pers. comm.) (i) Sequence of PAR6^{PDZ} with residues undergoing chemical exchange in response to positional exchange of L164 and K165, the conserved positively charged residue at the base of the ligand binding pocket (based on ref. [39], Figure 3C and Dr. B.F. Volkman, pers. comm.). (j) Significant Tiam-1^{PDZ} chemical shift changes upon binding of a peptide derived from Syndecan-1[40]. (k) Residues in GRIP1^{PDZ1} that form crucial interface contacts with its modulatory PDZ2 domain (only a few residues were tested based on crystallographic inspection)[41]. (l) Region of GRIP-1^{PDZ6} shown to undergo a large conformational change in response to ligand binding, as identified by X-ray crystallography[42]. (m) Aggregate evidence for conformational or energetic coupling to the ligand at positions not in direct contact with the ligand (allosteric, minimum distance between C, N, O, or S atoms > 5 Å in PDB entry 2VWR). Open circles: supported by four or five studies; filled circles: at least six studies (n) Same for residues in direct contact with the ligand.

Experiment	Protein*	Voltage (kV)†	Pulse duration (ns)†	X-ray delay (ns)	EF-pulses‡ per frame	Number of frames§	Total # EF-pulses	Assessment
2-03	Lysozyme	5.0	200	150	5	154	770	Too mosaic
(same)		8.0	200	60	5	63	315	
2-05	Lysozyme	8.0	200	150	5	62	310	Multiple lattices
2-06	Lysozyme	8.0	200	150	5	61	305	Multiple lattices
(same)		8.0	200	60	5	70	355	
2-15	Syntenin^{PDZ2}	6.0	500	450	5	63	315	Multiple lattices
2-17	LNX2^{PDZ2}	8.0	200	150	10	62	620	Multiple lattices
2-18	LNX2^{PDZ2}	8.0	200	150	7	62	434	Multiple lattices
2-22	LNX2^{PDZ2}	8.0	200	150	7	63	441	Good, limited
(same)		8.0	500	450	7	62	434	completeness
(same)		8.0	1,000	950	7	9	63	Explosion
2-56	Lysozyme	4.0	200	150	7	61	427	Multiple lattices
(same)		5.0	200	150	7	3	21	Multiple lattices
(same)		8.0	200	150	7	3	21	Explosion
2-64	Lysozyme	4.0	200	150	5	40	200	Twitching
(same)		5.0	200	150	1	61	61	Weak diffraction
(same)		8.0	200	150	1	71	71	Weak diffraction
2-66	Lysozyme	6.0	200	150	1	481	481	Weak diffraction
(same)		8.0	200	150	1	241	241	Weak diffraction
3-06	Lysozyme	6.4	200	150	5	80	400	Weak diffraction
3-08**	Lysozyme	6.4	200	150	3	181	543	Multiple lattices
3-09	Lysozyme	6.6	200	150	5	111	555	Multiple lattices
3-10	Lysozyme	6.4	200	150	3	120	360	Too mosaic
3-17**	PICK1^{PDZ}	3.0	200	150	5	182	910	Good
(same)		4.0	200	150	10	46	460	
3-24	LNX2^{PDZ2}	6.0	200	150	1	213	213	Good
3-25	LNX2^{PDZ2}	6.0	200	150	1	404	404	Good (**Table S7**)
3-35**	LNX2^{PDZ2}	6.0	250	50	1	363	363	**See Main Text.**
(same)		6.0	250	100	1	363	363	**See Main Text.**
(same)		6.0	250	200	1	363	363	**See Main Text.**
3-44	LNX2^{PDZ2}		200	150	1	182	182	Weak diffraction
3-48	LNX2^{PDZ2}		200	150	1	145	145	Weak diffraction
3-49	LNX2^{PDZ2}	5.0	200	150	1	235	235	Good (**Table S7**)
3-62	NaK2K	±1.0	200	150	4	198	792	Too Mosaic
(same)		-3.0	200	150	4	31	124	
(same)		-5.0	200	150	4	31	124	
(same)		-7.0	200	150	4	62	248	
(same)		-7.0	550	500	4	15	60	1,408 total
3-80**	NaK2K	-2.4	200	150	5	386	1,930	Too Mosaic
3-82	NaK2K	-5.0	200	150	8	91	728	Too Mosaic

TABLE S2 **Experimental parameters for select data sets**. Experiments were performed using "pink beam" radiation with a bandwidth of 5%[43]. The use of a pink beam places limits on acceptable crystal mosaicity to about 0.1°. As a result, diffraction patterns obtained were often unsuitable for further analysis. ∗ Most crystals were 50-100 μm thick based on visual inspection. † Electric field pulse duration. ‡ Note that multiple electric field (EF) and X-ray pulses were typically required per frame. § Frames with EF. Because OFF frames were also collected, the total number of X-ray exposures was typically twice or three times the number of EF pulses. ∗∗ Illustrated in Extended Data Figure 2.

Dataset	OFF	ON (50ns)	ON (100ns)	ON (200ns)
Number of images	361	361	361	359
Resolution*		100-1.8Å (1.88-1.8Å)		
		Single reflections		
R_{merge} (F^2)	0.092	0.079	0.095	0.081
R_{merge} (F)	0.053	0.046	0.055	0.047
$\langle F/\sigma_F \rangle$	39	46	38	45
Total observations	64,421	63,822	62,033	60,114
Unique observations	11,978	11,847	11,651	11,490
Redundancy	5.4	5.4	5.3	5.2
		Single and Harmonic reflections		
Unique observations	12,049	11,942	11,729	11,568
Completeness in P1*	74.9% (29.1%)	74.2% (27.8%)	72.9% (25.6%)	71.9% (24.2%)
Completeness in C2*	79.3% (38.6%)	78.7% (37.0%)	77.5% (34.3%)	77.0% (33.9%)

TABLE S3 **Data reductions statistics for LNX2^{PDZ2} time series data set**. Data were indexed, integrated, scaled and merged in Precognition (Methods). Completeness statistics were determined in CCP4 (mtzdump). ∗Note that, unlike in conventional data reduction software, only reflections passing several cutoffs are included in the final merged data set in Precognition. This biases estimates of completeness (down) and $\langle F/\sigma_F \rangle$ (up).

Data set		Residues with peaks near backbone O	*P**
OFF	**>+3.5 σ**	367	>0.1
	<-3.5 σ	339, 358, 409, 426	>0.1
	Both	--	>0.1
50 ns	**>+3.5 σ**	340, 347, 370, 379, 381, 399, 410, 414	>0.1
	<-3.5 σ	349, 381, 382, 385, 390, 398, 414, 427	>0.1
	Both	381, 414	>0.1
100 ns	**>+3.5 σ**	340, 357, 358, 359, 365, 370, 378, 379, 382, 384, 408, 409, 410, 414, 420	0.002
	<-3.5 σ	335, 336, 340, 355, 357, 358, 362, 382, 398, 415, 420	0.05
	Both	340, 357, 358, 382, 420	0.01
200 ns	**>+3.5 σ**	340, 362, 370, 378, 379, 382, 384, 409, 410, 414	>0.1
	<-3.5 σ	337, 350, 355, 357, 358, 362, 365, 382, 391, 394, 397, 404, 410, 415, 416	0.007
	Both	362, 382, 409, 410	0.09

TABLE S4 **Occurrence of internal difference density peaks near backbone oxygen atoms**. ∗Probability that at least this many residues will have peaks of the indicated type near backbone oxygen atoms, based on binomial sampling among the observed peaks in each internal difference electron density map. That is, the increased map variance and increased number of peaks at large deviations from zero are, *a priori*, excluded from causing the significance of obtained results.

Deviation (σ)	Nearest Residue	Near backbone (<1.5 Å)?
5.25	N384	Y
5.00	S410	N
4.93	S410	Y
4.89	L342	N
4.88	D394	N
4.87	V356	N
4.81	R357	N
4.76	S382	Y
4.74	P362	Y
4.67	R358	N
4.66	R380	N
4.60	R358	Y
4.56	D394	N
4.51	S383	Y
4.48	R413	N
4.42	D378	Y
4.42	L416	Y
4.41	V414	Y
4.36	N415	Y
4.34	R358	Y
4.32	--	N
4.29	R386	N
4.28	Y397	N
4.27	E371	N
4.24	--	N
4.19	Y397	Y
4.19	E401	Y
4.09	R357	Y
4.08	D385	N
4.08	S382	Y

TABLE S5 **Internal difference electron density peaks at 200 ns**. Shown are the 30 strongest internal difference electron density peaks. Note that each peak occurs twice with positive and twice with negative sign when using the C2 unit cell. Hence, we report peak strengths as positive numbers. The location of peaks was determined in Coot[44] using a map sampled at 0.3 Å (grid sampling rate = 3). The symbol – indicates that no residue atoms were found within 3 Å. We find 15 of 30 peaks near the protein backbone (expected by chance: 8.9; p = 0.007). We find 14 out of 28 peaks near charged residues (p = 0.012 by simple counting; p = 0.047 by overall residue Van der Waals volumes). Note that the standard deviation of the 200 ns map is 1.3x larger than for the OFF map, such that the for the highest peak 5.25 $\sigma_{ON} \approx 6.88\ \sigma_{OFF}$.

Deviation (σ)	Nearest Residue	Near backbone (1.5 Å)?
4.75	R413	N
4.65	Y397	N
4.61	R413	N
4.31	K423	N
4.29	--	N
4.27	Q339	N
4.21	L428	N
4.20	Q408	N
4.17	E412	N
4.15	Q339	Y
4.11	Q339	N
4.10	--	N
4.10	I426	N
4.08	E349	N

TABLE S6 **Internal difference electron density peaks for OFF data**. Shown are the internal difference electron density (DED) peaks above 4.08 for comparison with Table S5 (determined in the same manner). Localization near charged residues is not statistically significant ($p > 0.1$), while peaks are biased away from the protein backbone ($p = 0.99$).

Dataset	OFF			ON (150 ns)		
	Crystal e25	Crystal e49	Merged*	Crystal e25	Crystal e49	Merged
Number of images	218	180	398	212	180	392
Resolution*			100-1.8Å (1.88-1.8Å)			
			Single reflections			
R_{merge} $(F^2)^{\#}$	0.103	0.095	0.096	0.099	0.098	0.107
R_{merge} $(F)^{\#}$	0.056	0.055	0.051	0.055	0.057	0.054
$\langle F/\sigma_F \rangle$	28	32	43[b]	29	30	39[b]
Total observations	27,973	29,671	57,644	22,409	29,033	51,442
Unique observations	9,668	11,018	n/a	7,966	10,898	n/a
Redundancy**	2.9	2.7	4.8	2.8	2.7	4.5
			Single and Harmonic reflections			
Unique observations	9,721	11,099	11,899	8,037	10,960	11,456
Completeness in P1*,[a]	61.2% (15.7%)	69.8% (25.8%)	75.0% (31.3%)	50.5% (5.40%)	68.9% (24.4%)	72.2% (26.3%)
Completeness in C2*,[a]	67.8% (23.0%)	77.5% (36.4%)	79.7% (41.8%)	57.3% (8.7%)	76.8% (35.9%)	78.0% (37.7%)

TABLE S7 **Data reduction statistics for two additional crystals of LNX2^{PDZ2} and their merged data set (referred to as dataset 2)**. Data for crystals e25 and e49 were cut at 2 and 3 sigma, respectively, for merging in Epinorm. ∗Merged reflections (of each crystal separately) were merged in Matlab with weights based on their associated errors. ∗∗For data merged from both crystals, reported redundancy based on single and harmonic reflections instead. #For data merged from both crystals, we report the R factor for merging between these two data sets, unweighted, relative to unweighted mean; weighted $R_{merge}(F)$ are 0.037 and 0.035 for OFF and ON data, respectively. (a) Completeness in P1 after removal of reflections forbidden by residual translational symmetry; completeness calculated using ccp4/6.4.0 mtzdump. (b) Geometric means (arithmetic means ∼90, dominated by outliers).

III. Legends for Supplementary Online Materials

A. PyMOL session S1: Internal electron density difference map shown on the OFF structure. The difference map corresponds to Figure 3 of the main text. Meshes are contoured at $\pm 3.5\ \sigma_{OFF}$ (light red (+), light blue (−)) and $\pm 4.5\ \sigma_{OFF}$ (dark red (+), dark blue (−)). The map covers ten unit C2 cells, showing several OFF models to indicate their relative positions in the crystal lattice. Note that the internal electron density difference in this representation has equal magnitude and opposite sign. Shown is an orthoscopic view to highlight the overall pattern of internal electron density difference. The C-terminal portion of a symmetry mate acts as a ligand for the PDZ molecule; this is indicated on the sand-colored molecule in yellow stick bonds.

B. PyMOL session S2: Superimposed *up*, *down*, and OFF models and $2F_o - F_c$ electron density. Models were superimposed using the command "super" in PyMOL, based on C, C_α, and N atoms of residues 338-356, 362-380, 384-408 and 412-419; that is, excluding N- and C-terminal regions and parts of the 2-3, 1-4 and 2-6 loops displaying larger conformational changes. Shown are the non-hydrogen protein atoms, and water molecules with B factors less than 20 Å^2. Meshes indicate electron density levels of 1.0, 1.5 and 2.0 σ within 1.5 Å of displayed atoms. Ligands (C-terminal regions of symmetry mates) are shown as stick models.

C. PyMOL session S3: Superimposed *up*, *down*, and OFF models and $2F_o - F_c$ electron density for a composite omit map calculated with iterative refinement. Models and densities are presented as for PyMOL session S2.

D. PyMOL session S4: $2F_o - F_c$ electron density obtained for refinement against extrapolated structure factors in the reduced symmetry (P1) space group. Electron density (gray mesh at 1.5 σ) of the up (red) and down (blue) models as refined against extrapolated structure factors in the P1 space group. Ligands (C-terminal regions of symmetry mates) are shown as stick models (green and orange for down and up states, respectively). Water molecules with B factors less than 20 Å^2 are shown. Several additional symmetry-related molecules are also provided and/or shown to illustrate the relative positions of up and down molecules. The electron density covers the model with a 5 Å padding on all sides along unit cell axes.

E. Video S1: Destructive breakdown after dielectric seal failure. Movie of an experiment in which misalignment of electrodes led to dissociation of the protein crystal (lysozyme) from the bottom electrode, providing a conductive path around the crystal and leading to destructive arcing (dielectric breakdown). The video was recorded from a monitor with a piece of transparent adhesive tape with red dot indicating beam center, used in sample alignment.

F. Video S2: Establishing liquid junction between top counter electrode and the crystal. Movie showing the approach of the top electrode, brought in by manual control of a translation stage. The electrode is brought in sufficiently close to establish a liquid junction between the top electrode and the crystal.

IV. References

1. W Daseler, H J Steinhoff, and A Redhardt. "A new method for the determination of the permittivity of small samples in the microwave range and its application to hemoglobin single crystals". In: *J Biochem Biophys Methods* 22.1 (Jan. 1991), pp. 69–82.
2. LN Rashkovich, VA Smirnov, and EV Petrova. "Some dielectric properties of monoclinic lysozyme crystals". In: *Physics of the Solid State* 50.4 (2008), pp. 631–637.
3. R Fourme et al. "High-pressure protein crystallography (HPPX): instrumentation, methodology and results on lysozyme crystals". In: *Journal of synchrotron radiation* 8.5 (2001), pp. 1149–1156.
4. Amir Zamiri and Suvranu De. "Modeling the mechanical response of tetragonal lysozyme crystals". In: *Langmuir* 26.6 (Mar. 2010), pp. 4251–7. DOI: 10.1021/la9033222.
5. Zhongqiao Hu and Jianwen Jiang. "Electrophoresis in protein crystal: nonequilibrium molecular dynamics simulations". In: *Biophys J* 95.9 (Nov. 2008), pp. 4148–56. DOI: 10.1529/biophysj.108.140160.
6. Morozova TYa et al. "Ionic conductivity, transference numbers, composition and mobility of ions in cross-linked lysozyme crystals". In: *Biophys Chem* 60.1-2 (May 1996), pp. 1–16.
7. Heinz-Jürgen Steinhoff. "Thermophysical properties of protein crystals: thermal diffusivity measurements of methemoglobin single crystals using a dielectric heating technique". In: *Thermochimica Acta* 141 (1989), pp. 235–243.
8. R M Stroud and E B Fauman. "Significance of structural changes in proteins: expected errors in refined protein structures". In: *Protein Sci* 4.11 (Nov. 1995), pp. 2392–404. DOI: 10.1002/pro.5560041118.
9. T C Terwilliger and J Berendzen. "Difference refinement: obtaining differences between two related structures". In: *Acta Crystallogr D Biol Crystallogr* 51.Pt 5 (Sept. 1995), pp. 609–18. DOI: 10.1107/S0907444994013247.
10. M Krieger, L_M Kay, and RM Stroud. "Structure and specific binding of trypsin: comparison of inhibited derivatives and a model for substrate binding". In: *Journal of molecular biology* 83.2 (1974), 209IN15219–218230.
11. U K Genick et al. "Structure of a protein photocycle intermediate by millisecond time-resolved crystallography". In: *Science* 275.5305 (Mar. 1997), pp. 1471–5.
12. Jason Tenboer et al. "Time-resolved serial crystallography captures high-resolution intermediates of photoactive yellow protein". In: *Science* 346.6214 (Dec. 2014), pp. 1242–6. DOI: 10.1126/science.1259357.
13. A T Brünger. "Free R value: cross-validation in crystallography". In: *Methods Enzymol* 277 (1997), pp. 366–96.
14. James E Knapp et al. "Allosteric action in real time: time-resolved crystallographic studies of a cooperative dimeric hemoglobin". In: *Proc Natl Acad Sci U S A* 103.20 (May 2006), pp. 7649–54. DOI: 10.1073/pnas.0509411103.
15. Vukica Šrajer et al. "Protein conformational relaxation and ligand migration in myoglobin: a nanosecond to millisecond molecular movie from time-resolved Laue X-ray diffraction". In: *Biochemistry* 40.46 (2001), pp. 13802–13815.
16. W J Ray Jr et al. "Removal of salt from a salt-induced protein crystal without cross-linking. Preliminary examination of "desalted" crystals of phosphoglucomutase by X-ray crystallography at low temperature". In: *Biochemistry* 30.28 (July 1991), pp. 6866–75.
17. Dominique Bourgeois et al. "Time-resolved methods in biophysics. 6. Time-resolved Laue crystallography as a tool to investigate photo-activated protein dynamics". In: *Photochem Photobiol Sci* 6.10 (Oct. 2007), pp. 1047–56. DOI: 10.1039/b704249c.
18. Juan Sanchez-Weatherby et al. "Improving diffraction by humidity control: a novel device compatible with X-ray beamlines". In: *Acta Crystallogr D Biol Crystallogr* 65.Pt 12 (Dec. 2009), pp. 1237–46. DOI: 10.1107/S0907444909037822.
19. Yevgeniy Kalinin et al. "A new sample mounting technique for room-temperature macromolecular crystallography". In: *Journal of applied crystallography* 38.2 (2005), pp. 333–339.
20. James B Sumner. "The isolation and crystallization of the enzyme urease preliminary paper". In: *Journal of Biological Chemistry* 69.2 (1926), pp. 435–441.
21. P J Kasvinsky and N B Madsen. "Activity of glycogen phosphorylase in the crystalline state". In: *J Biol Chem* 251.21 (Nov. 1976), pp. 6852–9.
22. L A Sluyterman and M J de Graaf. "The activity of papain in the crystalline state". In: *Biochim Biophys Acta* 171.2 (Feb. 1969), pp. 277–87.
23. Marilynn S Doscher and Frederic M Richards. "The activity of an enzyme in the crystalline state: Ribonuclease S". In: *Journal of Biological Chemistry* 238.7 (1963), pp. 2399–2406.
24. B F Rasmussen et al. "Crystalline ribonuclease A loses function below the dynamical transition at 220 K". In: *Nature* 357.6377 (June 1992), pp. 423–4. DOI: 10.1038/357423a0.
25. Teruya Nakamura et al. "Watching DNA polymerase make a phosphodiester bond". In: *Nature* 487.7406 (July 2012), pp. 196–201. DOI: 10.1038/nature11181.
26. A Mozzarelli et al. "Cooperative oxygen binding to scapharca inaequivalvis hemoglobin in the crystal". In: *J Biol Chem* 271.7 (Feb. 1996), pp. 3627–32.
27. J Jegan Roy and T Emilia Abraham. "Strategies in making cross-linked enzyme crystals". In: *Chem Rev* 104.9 (Sept. 2004), pp. 3705–22. DOI: 10.1021/cr0204707.

28. Vipin Agarwal et al. "Protein side-chain dynamics as observed by solution- and solid-state NMR spectroscopy: a similarity revealed". In: *J Am Chem Soc* 130.49 (Dec. 2008), pp. 16611–21. DOI: 10.1021/ja804275p.

29. David D Boehr et al. "The dynamic energy landscape of dihydrofolate reductase catalysis". In: *Science* 313.5793 (Sept. 2006), pp. 1638–42. DOI: 10.1126/science.1130258.

30. B Alberts. "The cell as a collection of protein machines: preparing the next generation of molecular biologists". In: *Cell* 92.3 (Feb. 1998), pp. 291–4.

31. Jimin Pei, Bong-Hyun Kim, and Nick V Grishin. "PROMALS3D: a tool for multiple protein sequence and structure alignments". In: *Nucleic Acids Res* 36.7 (Apr. 2008), pp. 2295–300. DOI: 10.1093/nar/gkn072.

32. A.M. Poole. "Collective structural models in proteins: A case study in the PDZ domain". PhD thesis. UT Southwestern Medical Center, 2012.

33. Richard N McLaughlin Jr et al. "The spatial architecture of protein function and adaptation". In: *Nature* 491.7422 (Nov. 2012), pp. 138–42. DOI: 10.1038/nature11500.

34. Xiaogang Niu et al. "Interesting structural and dynamical behaviors exhibited by the AF-6 PDZ domain upon Bcr peptide binding". In: *Biochemistry* 46.51 (Dec. 2007), pp. 15042–53. DOI: 10.1021/bi701303p.

35. Yifei Kong and Martin Karplus. "Signaling pathways of PDZ2 domain: a molecular dynamics interaction correlation analysis". In: *Proteins* 74.1 (Jan. 2009), pp. 145–54. DOI: 10.1002/prot.22139.

36. Ernesto J Fuentes, Channing J Der, and Andrew L Lee. "Ligand-dependent dynamics and intramolecular signaling in a PDZ domain". In: *Journal of molecular biology* 335.4 (2004), pp. 1105–1115.

37. G Kozlov, K Gehring, and I Ekiel. "Solution structure of the PDZ2 domain from human phosphatase hPTP1E and its interactions with C-terminal peptides from the Fas receptor". In: *Biochemistry* 39.10 (Mar. 2000), pp. 2572–80.

38. Lieke C J van den Berk et al. "An allosteric intramolecular PDZ-PDZ interaction modulates PTP-BL PDZ2 binding specificity". In: *Biochemistry* 46.47 (Nov. 2007), pp. 13629–37. DOI: 10.1021/bi700954e.

39. Dustin S Whitney et al. "Allosteric activation of the Par-6 PDZ via a partial unfolding transition". In: *Journal of the American Chemical Society* 135.25 (2013), pp. 9377–9383.

40. Tyson R Shepherd et al. "The Tiam1 PDZ domain couples to Syndecan1 and promotes cell-matrix adhesion". In: *J Mol Biol* 398.5 (May 2010), pp. 730–46. DOI: 10.1016/j.jmb.2010.03.047.

41. Jiafu Long et al. "Supramodular nature of GRIP1 revealed by the structure of its PDZ12 tandem in complex with the carboxyl tail of Fras1". In: *J Mol Biol* 375.5 (Feb. 2008), pp. 1457–68. DOI: 10.1016/j.jmb.2007.11.088.

42. Young Jun Im et al. "Crystal structure of GRIP1 PDZ6-peptide complex reveals the structural basis for class II PDZ target recognition and PDZ domain-mediated multimerization". In: *J Biol Chem* 278.10 (Mar. 2003), pp. 8501–7. DOI: 10.1074/jbc.M212263200.

43. T Graber et al. "BioCARS: a synchrotron resource for time-resolved X-ray science". In: *J Synchrotron Radiat* 18.Pt 4 (July 2011), pp. 658–70. DOI: 10.1107/S0909049511009423.

44. P Emsley et al. "Features and development of Coot". In: *Acta Crystallogr D Biol Crystallogr* 66.Pt 4 (Apr. 2010), pp. 486–501. DOI: 10.1107/S0907444910007493.